Post-Failure Modes for Steel Sheeting Subject to Concentrated Load (Web Crippling) and Bending Moment

H. Hofmeyer
J.G.M. Kerstens
H.H. Snijder
M.C.M. Bakker
Eindhoven University of Technology, Faculty of Architecture, Department of Structural Design.

Cold-formed trapezoidal sheeting of thin steel plate is a very popular product for building construction. It combines low weight and high strength and is economical in use. To increase the insight into the behaviour of the sheeting, this article presents new experiments in which first-generation sheeting behaviour is studied under combined concentrated load and bending. The experiments show that after ultimate load, three different post-failure modes occur. Mechanical models have been developed for the three post-failure modes. These models can help to explain why a certain post-failure mode occurs.

***Keywords*: steel sheeting, concentrated load, web crippling, bending moment, post-failure.**

1 Introduction

Cold-formed trapezoidal sheeting of thin steel plate is a very popular product for building construction. It combines low weight and high strength and is economical in use. Figure 1 shows a photo of sheeting used for roof construction.

First generation sheeting is usually a rolled plate without any stiffeners. Second generation sheeting has stiffeners in the longitudinal direction only. Third generation sheeting also has stiffeners in the transverse direction. In this article, only first generation sheeting is investigated, although second and third generation sheetings are widely used. The reason for this limitation is that it is important to first understand the behaviour of the relatively simple first generation sheeting.

Next to trapezoidal sheeting, sheet sections will be introduced later in this article. Here, only their definitions are given (see figure 2). Trapezoidal sheeting is folded (rolled) plate with several webs and flanges. A sheet section is a combination of one bottom flange, two webs, and two half top flanges. Constraints are applied at the edges of the two half top flanges to let this sheet section behave like infinitely wide sheeting. A hat section is a sheet section without constraints at the edges of the two half top flanges.

Thus, it may behave differently from trapezoidal sheeting and sheet sections. At an interior support, sheeting is subjected to a concentrated load F and a bending moment M as shown in figure 3.

Fig. 1. Sheeting used for roof construction.

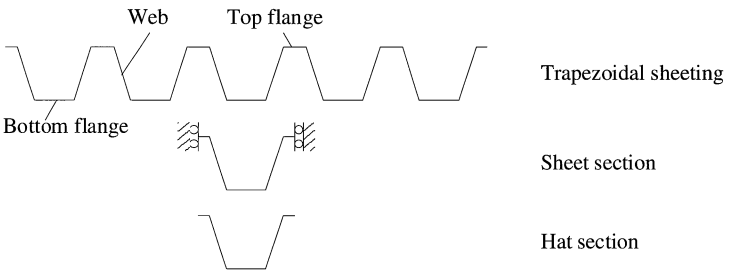

Fig. 2. Definitions of trapezoidal sheeting, sheet sections, and hat sections.

At this moment, design rules do not provide sufficient insight in the failure behaviour of sheeting subjected to a concentrated load and a bending moment. To increase the insight in sheeting behaviour, in this article new experiments are presented in section 2. The experiments show three post-failure modes after ultimate load (a post-failure mode is a specific type of failure after ultimate load). In section 3, three mechanical models are presented to predict the ultimate load for every post-failure mode. The quality of the models is studied by comparing their predictions with experimental results (besides these models, also one very good model was developed for two post-failure modes at the same time, see [3]). Section 4 shows how the mechanical models increase the insight in sheeting behaviour. This by studying which mechanical model predicts the lowest load for changing sheeting variables. Section 5 presents the conclusions. In general, additional information to this article can be found in references [1, 2, 3, 4].

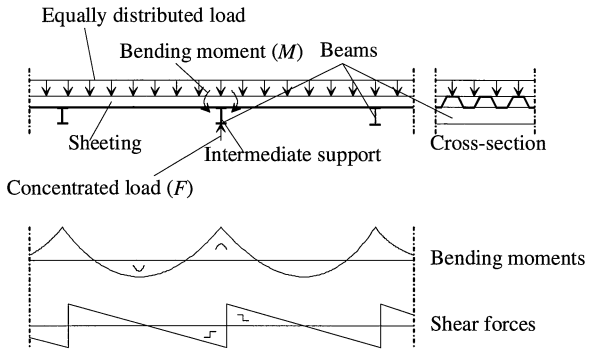

Fig. 3. Longitudinal section and cross-section of sheeting.

2 Experiments

In the experiments presented in this article, sheet sections are tested in a three-point bending test. The sheet sections are chosen to represent the situation in practice for two aspects: the sheet section cross-section variables (sheet section height for example) and the loading conditions (*M/F* ratios and $M^*F/M_u^*R_u$ (η) ratios). Both should be similar for the experiments and the situation in practice. M_u is the ultimate bending moment and R_u the ultimate concentrated load the sheeting can bear.

All sheet sections, with their nominal values, are shown in figure 4. The variable L_{span} stands for the span length, θ_w for the angle between web and flange [deg.], b_{bf} is the bottom flange width [mm]. The variable r_{bf} stands for the bottom corner radius [mm] and L_{lb} for the load-bearing plate width [mm]. The sheet sections having a length of 600 mm (test 1 to 15) were not part of the experiments originally. They were added later. Their aim was to be able to compare the experiments in this article (long span lengths) with the experiments of Bakker (short lengths) [5]. For the sheet sections the η ratio is 0.45 to 3.60 and the *M/F* ratio ranges from 125 to 575 mm. In figure 5, these *M/F*-ratios and η ratios are shown and the experimental values do represent the situation in practice.

The experimental research uses a three-point bending test configuration to test the sheet sections. Instead of a normal experimental set-up for three-point bending tests, an upside down set-up was used. This set-up made it possible to investigate the deformation of the cross-section by making castings of the inner cross-section during deformation. The test rig (mechanical properties) is shown in figure 6. A hydraulic jack is connected to a load-bearing plate, which loads the sheet section. The sheet section is supported by two support strips that are connected to four support rods by two support bars. The support rods are connected to a rigid beam that is the base of the test rig. Strips are fixed to the sheet section to avoid spreading of the webs and sway of the cross-section.

L_{span}	θ_w	b_{bf}	r_{bf} / L_{lb}	1			3		5		10		
				50	100	150	50	100	50	100	50	100	150
600	90	100		1			4			5			
	70	100		2					6		7-13		
	50	40		3									
		100									14	15	
1000	90	100			26								
	70	40			28								
		100			27								
	50	100						16-21					
1200	90	100		22					32			35	
	70	40			29								
		100			23			30	33				36,37
	50	40		24		25			34				
		100					31				38		
1400	50	40			39								
1800	90	100			40			43		46,47			
	70	100			41			44		48,49		51	
	50	40			42			45				52	
		100								50			
2400	90	100						55		58,59		68	
	70	100			53			56		60		70	69
	50	40			54					61-67			
		100						57				71	72

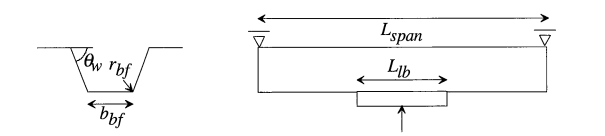

Fig. 4. Experiments.

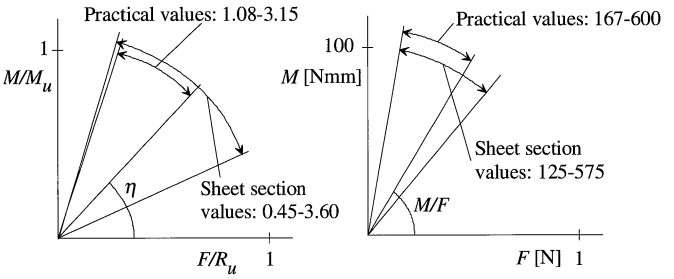

Fig. 5. Practical and experimental values.

The experiments show three different yield line patterns after ultimate load (figure 7). Before ultimate load, no yield lines are visible. The differences for the three yield line patterns are as follows. Yield line pattern II shows yield lines -bold lines (a) and (b)- directly on both sides of the bottom corners. The other two patterns show no yield lines on the bottom corner, but one yield line in the web (a) and one in the flange (b). The third pattern is asymmetrical in the longitudinal direction. The other two patterns are symmetrical. Every yield line pattern is accompanied by a specific load versus web crippling deformation curve, see figure 7 at the bottom.

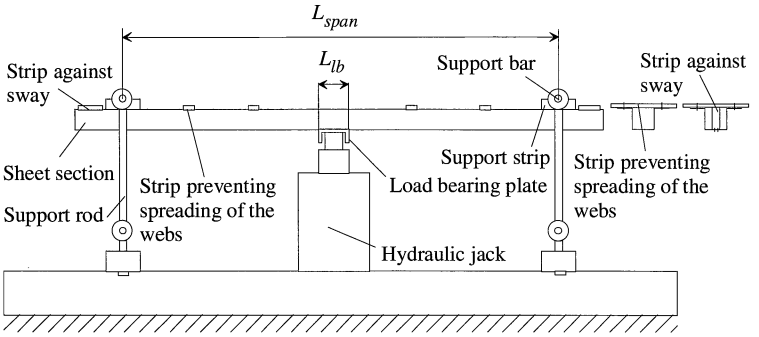

Fig. 6. Test rig.

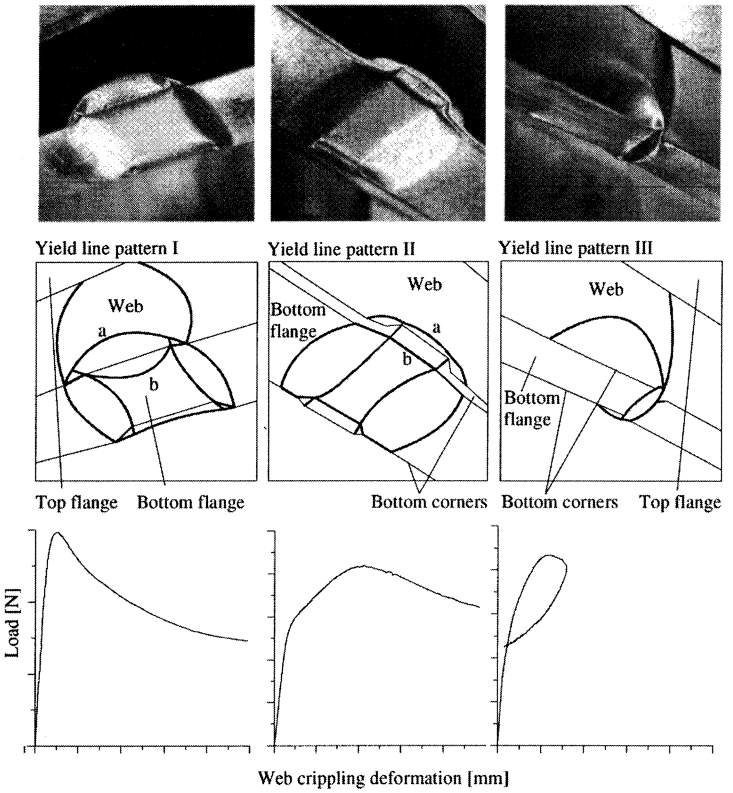

Fig. 7. Yield line patterns and accompanying load deformation curves.

Yield line pattern II and the accompanying load deformation curve are defined as a rolling post-failure mode. This is because the yield lines at the bottom corner roll through the web and flange. Yield line pattern I and the accompanying load deformation curve are defined as a yield arc post-failure mode. This is because an arc-like shape develops in the web. Yield line pattern III and the accompa-

nying load deformation curve are defined as a yield eye post-failure mode, as an eye-like shape develops in the bottom flange.

In figure 8, post-failure modes are shown for all tests. The character "A" stands for a yield arc post-failure mode, the character "E" stands for a yield eye post failure mode. "R" stands for a rolling post-failure mode, and "A>R" stands for a yield arc post-failure mode that is followed by a rolling post-failure mode. Finally, "A>E" stands for a yield arc post-failure mode that is followed by a yield eye post-failure mode.

L_{span}	θ_w	b_{bf}	r_{bf} / L_{lb}	1			3		5		10		
				50	100	150	50	100	50	100	50	100	150
600	90	100		A>R			A>R			A			
	70	100		A>R					A>R		R*		
	50	40		A>R									
		100									A>R	A>R	
1000	90	100			A								
	70	40			A								
		100			A								
	50	100						A*					
1200	90	100		A					A			A	
	70	40			A								
		100			A			A	A				A,A
	50	40		A		A			A				
		100					A>R				A>R		
1400	50	40			A>E								
1800	90	100			E			A		A,A			
	70	100			A			A		A,A		A	
	50	40			A			A				A	
		100								A			
2400	90	100						A>E		A,A		A	
	70	100			A			A>E		A		A	A>E
	50	40			E					E**			
		100						A				A	A>E

* More experiments in one field.

Fig. 8. Post-failure modes for experiments.

3 Post-failure models

The post-failure models are used to predict which post-failure mode occurs: all post-failure models in this section predict the mode initiation load F_{imec}. This is the intersection of curves describing elastic and plastic sheeting behaviour. For the yield arc and yield eye post-failure modes, load F_{imec} is a prediction for the ultimate load, see figure 9. For the rolling post-failure mode, figure 9 shows that F_{imec} is not a prediction of the ultimate load; it only predicts first plastic behaviour. The post-failure models are not used to predict the ultimate load. For this aim, an other model has been developed [3,4].

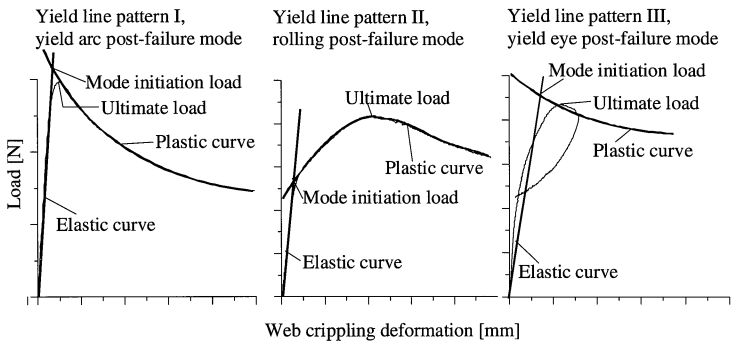

Fig. 9. Mode initiation and ultimate loads for all three post-failure modes.

3.1 *Mechanical model for the yield arc post-failure mode*

Elastic behaviour

In 1995, Vaessen developed mechanical models to predict the elastic relationship between load and web crippling deformation for sheet sections [6,7]. A part of one of his models can be used to predict the elastic load F_e on the load-bearing plate for a certain indentation of the cross-section (web crippling deformation Δh_w):

$$F_e = \frac{EI(3b_{bf} + 2b_w)\Delta h_w}{r_{ibf}^2 \sin^2(\theta_w) b_w \left(b_{bf} - \frac{4}{3} r_{ibf} \sin(\theta_w) \right)}, \text{ where } I = \frac{1}{12} L_{lb} t^3 \quad (1)$$

The formula is valid for first-order elastic behaviour for a part of the sheet section (defined as "modelled cross-section"), as shown in figure 10. Flange or web buckling is not taken into account.

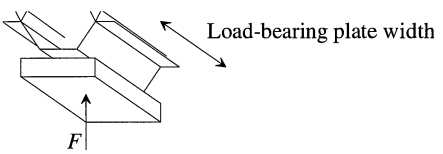

Fig. 10. Modelled cross-section.

Plastic behaviour

For the yield arc post-failure mode, the plastic behaviour of the cross-section is modelled as shown in figure 11. Making use of the principle of virtual displacements, the plastic load F_p related to the web crippling deformation Δh_w is as follows:

$$F_p = 2\frac{2}{\sqrt{3}}\frac{f_y t^2}{4} L_{lb}\left(\frac{\delta\varphi_a}{\delta\Delta h_w}+\frac{\delta\varphi_b}{\delta\Delta h_w}+\frac{\delta\varphi_c}{\delta\Delta h_w}\right) \tag{2}$$

$$\text{where}\quad \frac{\delta\varphi_a}{\delta\Delta h_w} = \frac{\left(\frac{\delta x}{\delta\Delta h_w}\right)}{b_w - L_w} + \frac{\left(L_w^2 - (b_w - L_w)^2 - x^2\right)\left(\frac{\delta x}{\delta\Delta h_w}\right)}{2(b_w - L_w)x^2} \Bigg/ \sqrt{1 - \frac{\left(L_w^2 - (b_w - L_w)^2 - x^2\right)^2}{4(b_w - L_w)^2 x^2}} + \frac{\sec\theta_w}{1 + \frac{(h_w - \Delta h_w)^2 \sec^2\theta_w}{b_w^2}} \tag{3}$$

$$\text{and}\quad x = \sqrt{(h_w - \Delta h_w)^2 + b_w^2 \cos^2\theta_w} \tag{4}$$

F_p = load for plastic behaviour [N].
f_y = steel yield strength [N/mm^2].
L_w = distance between yield lines [mm].
φ_i = rotation yield line i [rad.].
x = substitute variable.

The factors $\delta\varphi_b/\delta\Delta h_w$ and $\delta\varphi_c/\delta\Delta h_w$ are just as complex as factor $\delta\varphi_a/\delta\Delta h_w$ and can be found in section 3.2 of report [2]. Distance L_w is predicted by a method presented in section 4.3 of this report [2].

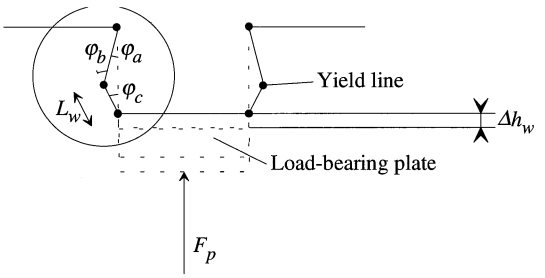

Fig. 11. Plastic behaviour for modelled cross-section.

Intersection of elastic and plastic curves

Formulae 2, 3, and 4 can be simplified [2]. Making the simplified formulae equal to formula 1 (see introduction section 3) yields the predicted ultimate load of the modelled cross-section. This load is defined as F_{csu}:

$$F_{csu} = \frac{-\alpha - \beta + \sqrt{4A\alpha h_w (b_w - L_w) L_w k + (\beta + \alpha)^2}}{2A(b_w - L_w)L_w} \quad (5)$$

$$k = \frac{EI(3b_{bf} + 2b_w)}{r_{ibf}^2 \sin^2(\theta_w) b_w \left(b_{bf} - \frac{4}{3} r_{ibf} \sin(\theta_w) \right)} \quad (6)$$

$$\alpha = f_y L_{lb} t^2 \quad (7)$$

$$\beta = kL_w (C + BL_w)(b_w - L_w) \quad (8)$$

$$A = 0.0624 \quad (9)$$

$$B = -0.0101 \quad (10)$$

$$C = 0.5633 \quad (11)$$

Correction 1 of the ultimate load prediction

Figure 13 shows that not only the modelled cross-section indents during loading, but also two parts adjacent to the modelled cross-section, over a length L_{bf}. The load needed to indent the cross-section equals F_{csu} / L_{lb} per mm. Therefore, the load needed to indent a piece with width L_{bf} equals $F_{csu} * L_{bf} / L_{lb}$. Because the indentation equals Δh_w at one end and zero at the other, it is estimated that only half the load is needed. Because there are two parts, the load to deform the two parts adjacent to the load-bearing plate, load F_{2p}, simply equals:

$$F_{2p} = F_{csu} \frac{L_{bf}}{L_{lb}} \quad (12)$$

The ultimate load of the modelled cross-section F_{csu} can be corrected by adding the load F_{2p}.

Correction 2 of the ultimate load prediction

Figure 13 shows that yield lines occur in the bottom flange of the sheet section. These yield lines dissipate energy, like the yield lines in the modelled cross-section. The yield lines in the bottom flange

are shown in figure 12. For the moment, it is assumed that the bottom flange parts 1 and 3 do not rotate relative to each other.

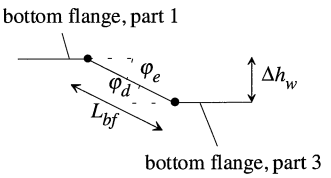

Fig. 12. Simple model to predict the force F_{ylbf} to deform the bottom flange.

The extra force needed to form the yield lines in the bottom flange F_{ylbf} can be predicted as follows:

$$\varphi_d = \varphi_e = \arcsin\frac{\Delta h_w}{L_{bf}} \tag{13}$$

$$\frac{\delta\varphi_d}{\delta\Delta h_w} = \frac{\delta\varphi_e}{\delta\Delta h_w} = \frac{1}{L_{bf}\sqrt{1-\left(\frac{\Delta h_w}{L_{bf}}\right)^2}} = \frac{1}{\sqrt{{L_{bf}}^2 - {\Delta h_w}^2}} \tag{14}$$

$$F_{ylbf} = 2\frac{2}{\sqrt{3}}\frac{{f_y t}^2}{4} b_{bf}\left(\frac{\delta\varphi_d}{\delta\Delta h_w} + \frac{\delta\varphi_e}{\delta\Delta h_w}\right) \tag{15}$$

The ultimate load of the modelled cross-section F_{csu} can be corrected by adding the load F_{ylbf}.

Correction 3 of the ultimate load prediction

The load on the modelled cross-section F_{cs} equals the load acting on the load-bearing plate F plus an extra force F_l due to indentation of the cross-section. Figure 13 illustrates this.

If the modelled cross-section deforms, yield lines develop in the bottom flange, which behave like hinges. Besides these yield lines, compressive forces develop in the bottom flange, due to the bending moment in the sheet section. These compressive forces, through the hinges, increase the force on the modelled cross-section. This increase of force strongly depends on the section length. Therefore, this effect will be defined as 'length effect'.

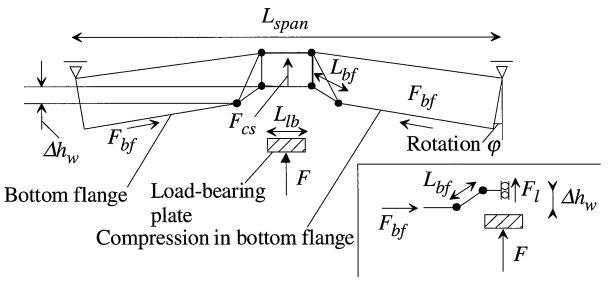

Fig. 13. Load at modelled cross-section F_{cs} equals load acting on load-bearing plate F plus an extra force F_l due to indentation of the cross-section.

First, virtual displacements are used to predict the internal and external incremental energy. During an incremental change of the modelled cross-section indentation Δh_w, the load F acting on the sheet section moves. Not only the distance Δh_w (which is only the case for the indented cross-section) but also for an extra displacement caused by the deflection of the sheet section. The incremental energy can be written as follows (using figure 13):

$$\delta E_{e1} = F_{cs}\delta\Delta h_w \tag{16}$$

$$\delta E_{e2} = F\left(\delta\Delta h_w + \delta\varphi\left(\frac{L_{span} - L_{lb}}{2}\right)\right) \tag{17}$$

δE_{e1} = incremental external energy cross-section only.
δE_{e2} = incremental external energy cross-section and sheet section deflection.
$\delta\Delta h_w$ = incremental cross-section indentation.
$\delta\varphi$ = incremental sheet section rotation.

Influences of stress on yield line energy dissipation are neglected and it is assumed that the yield line pattern does not change geometrically during deformation. Then, because both mentioned external energy terms should equal the incremental internal energy and internal energy is equal for both cases, we can derive the following:

$$\delta E_{e1} = \delta E_{e2} \Leftrightarrow$$

$$F_{cs}\delta\Delta h_w = F\left(\delta\Delta h_w + \delta\varphi\left(\frac{L_{span} - L_{lb}}{2}\right)\right) \Leftrightarrow F = \frac{F_{cs}\delta\Delta h_w}{\left(\delta\Delta h_w + \delta\varphi\left(\frac{L_{span} - L_{lb}}{2}\right)\right)} \Leftrightarrow$$

$$F = F_{cs}\frac{1}{\left(1 + \frac{\delta\varphi}{\delta\Delta h_w}\left(\frac{L_{span} - L_{lb}}{2}\right)\right)} = F_{cs} * f_{l1} \tag{18}$$

f_{l1}= length factor 1

The factor $\delta\varphi/\delta\Delta h_w$ is complex and can only be predicted with complicated formulae (report [2], Appendix 3, section 3.3). The ultimate load of the modelled cross-section F_{csu} is corrected by multiplying the load with factor f_{l1}.

Ultimate load F_u

The ultimate load is now found as follows:

$$F_u = (F_{csu} + F_{2p} + F_{ylbf})f_{l1} \tag{19}$$

Yield line distance L_{bf}

The distance between yield lines L_{bf} is shown in figure 13. The distance L_{bf} can be determined by varying L_{bf} and finding the minimum value for the ultimate load F_u (see [1,2] for more information):

$$L_{bf} = \sqrt{\frac{2f_y t^2 L_{lb} b_{bf}\, 2.601}{4F_{csu}}} \tag{20}$$

Summary

The ultimate load of a sheet section for the yield arc post-failure mode is predicted as follows:

Yield line distance L_w is predicted by a mechanical model presented in section 4.3 of report [2].
The ultimate load for the modelled cross-section F_{csu} is determined using formulae 5 to 11.
Distance L_{bf} is predicted by formula 20.
Load F_{2p} is predicted by formula 12.
Load F_{ylbf} is predicted by formulae 13 to 15.
Factor f_{l1} is calculated by formula 18.
Load F_u is found by formula 19.

3.2 *Mechanical model for the rolling post-failure mode*

Elastic behaviour

Elastic behaviour is the same for sheet sections failing by the yield arc and rolling post-failure modes. Therefore, the formula presented in section 3.1 can be used.

Plastic behaviour

The plastic behaviour of the cross-section is modelled as shown in figure 14. Making use of the principle of virtual displacements, the plastic load F_p related to the cross-section indentation Δh_w equals:

$$F_p = 2\frac{\delta u_a}{\delta \Delta h_w}\frac{1}{r_{bf}}\frac{2}{\sqrt{3}}\frac{{f_y t}^2}{4}L_{lb} + 2\frac{\delta u_b}{\delta \Delta h_w}\frac{1}{r_{bf}}\frac{2}{\sqrt{3}}\frac{{f_y t}^2}{4}L_{lb} + 2\frac{\delta \varphi_c}{\delta \Delta h_w}\frac{2}{\sqrt{3}}\frac{{f_y t}^2}{4}L_{lb} \tag{21}$$

$$\frac{\delta u_a}{\delta \Delta h_w} = \frac{\sin(\theta_w + \varphi_c)}{1-\cos(\theta_w + \varphi_c)} \tag{22}$$

$$\frac{\delta u_b}{\delta \Delta h_w} = \frac{\sin(\theta_w + \varphi_c)}{1-\cos(\theta_w + \varphi_c)} + \frac{r_{bf}}{b_{wfl} - \Delta b_{wfl}} \tag{23}$$

$$\Delta b_{wfl} = \frac{b_{wfl}\left(\cos\theta_w - \cos(\theta_w + \varphi_c)\right) + r_{bf}\left(\sin\theta_w + \varphi_c - \sin(\theta_w + \varphi_c)\right)}{1-\cos(\theta_w + \varphi_c)} \tag{24}$$

Calculating φ_c as:

$$\varphi_c = -\frac{\Delta h_w \sin\left(\frac{\theta_w}{2}\right)}{\Delta h_w \cos\left(\frac{\theta_w}{2}\right) - b_w \sin\left(\frac{\theta_w}{2}\right)} \tag{25}$$

δu_i= incremental movement of yield line *i*.

r_{bf}= corner radius bottom flange.

Δb_w= change of web width b_w.

More information can be found in the report [2], Appendix 2, section 2.3.

Intersection of elastic and plastic curves

Formulae 1 and 21 can be set equal. The solution is shown by formula 26. The variable k is given by formula 6.

$$F_{csu} = -k\frac{2b_w\left(\frac{L_{lb}2{f_y t}^2}{\sqrt{3}r_{bf}}\right)\cos\left(\frac{\theta_w}{2}\right)\sin\left(\frac{\theta_w}{2}\right)}{-b_w k - \left(\frac{L_{lb}2{f_y t}^2}{\sqrt{3}r_{bf}}\right) + b_w k\cos(\theta_w)} \tag{26}$$

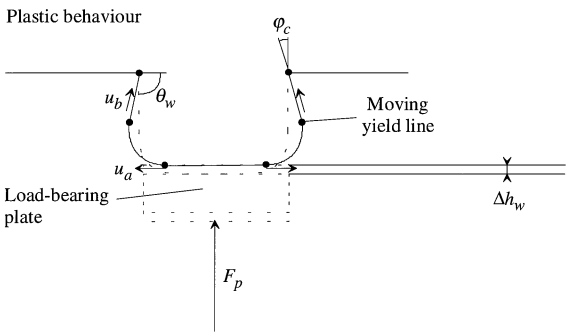

Fig. 14. Rolling post-failure mode, plastic behaviour.

Corrections of the ultimate load prediction

The corrections of the ultimate load prediction for the rolling post-failure mode are the same as for the yield arc post-failure mode (section 3.1).

Summary

The ultimate load of a sheet section for the rolling post-failure mode is predicted as follows:

The ultimate load for the modelled cross-section F_{csu} is determined using formula 6 and 26.
Distance L_{bf} is predicted by formula 20.
Load F_{2p} is predicted by formula 12.
Load F_{ylbf} is predicted by formulae 13 to 15.
Factor f_{l1} is calculated by formula 18.
Load F_u is found by formula 19.

3.3 *Mechanical model for the yield eye post-failure mode*

Elastic behaviour

Elastic behaviour is the same for sheet sections failing by the yield arc and yield eye post-failure modes. Therefore, the formula presented in section 3.1 can be used.

Plastic behaviour

The yield eye post-failure mode has an eye-like yield line pattern located on the bottom flange (see also section 2). In 1981, Murray and Khoo presented a paper that discussed some models to describe the behaviour of simple yield line patterns [8]. One of these patterns was called a flip-disc pattern and has a strong geometrical similarity to the eye-like yield line pattern of the yield eye post-failure mode. Figure 15 shows a thin-walled plate compressed by a force F_{bf}.

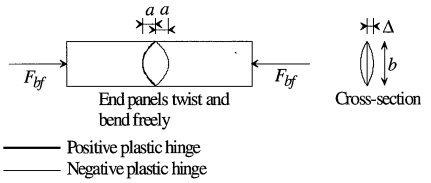

Fig. 15. Thin-walled plate. Flip-disc pattern.

According to Murray and Khoo, the force F_{bf} can be predicted using the following formula:

$$F_{bf} = \frac{f_y t b}{6}\left[1 - \frac{2\Delta}{t} + \sqrt{\left(\frac{2\Delta}{t}\right)^2 + 1 - \frac{6\Delta}{t\left(1+4a^2/b^2\right)} + 4\sqrt{\left(\frac{3\Delta}{2t\left(1+4a^2/b^2\right)}\right)^2 + 1}}\right] \tag{27}$$

With:

a =0.2b.

F_{bf} = compressive force [N].

Δ = flip-disc out-of-plane deflection [mm].

b = plate width [mm].

a = flip-disc half width [mm].

t = steel plate thickness [mm].

f_y = steel yield strength [N/mm^2].

Intersection of elastic and plastic curves

Formula 1 describes the relationship between the concentrated load F acting on the sheet section and the sheet section web crippling deformation Δh_w. Formula 27 defines the load F_{bf} acting on the bottom flange needed to form a plastic mechanism for a certain flip-disc out-of-plane deflection Δ. Thus, elastic and plastic formulae have different load and deformation variables. A relationship between the load on the sheet section F and the load on the bottom flange F_{bf} should be developed. Furthermore a relationship between the elastic cross-section deformation variable Δh_w and the plastic flip-disc deformation variable Δ should be developed.

Cross-section deformation versus flip-disc deformation

Figure 16 shows a possible relationship for this: for elastic behaviour, it is assumed that a certain width adjacent to the modelled cross-section will deform like the modelled cross-section. This certain width is set equal to the distance $2a$ between yield lines in the bottom flange during plastic deformation. This leads to the following derivation:

$$\frac{2\Delta}{2a} = \frac{\Delta h_w}{2a} \Leftrightarrow \Delta = 0.5\Delta h_w \tag{28}$$

Δ = flip-disc out-of-plane deflection [mm].
Δh_w= web crippling deformation [mm].

Load at section versus load at bottom flange
Looking at figure 16 it can be seen that the external bending moment in the section equals:

$$M_e = \frac{FL_{span}}{4} \tag{29}$$

M_e = external bending moment [Nmm]
F = concentrated load of support on section [N]
L_{span}= span length [mm]

This gives the following assumptions:

[a] One concentrated load F models the load of the load-bearing plate.
[b] The flip-disc occurs in the position of this concentrated load, i.e. the location of highest bending moment.

The internal bending moment in the section can be derived as follows:

$$\frac{F_{bf}}{b_{bf}t} = \frac{M_i}{I_s}s \Leftrightarrow M_i = \frac{F_{bf}I_s}{b_{bf}s*t} \tag{30}$$

M_i = internal bending moment [Nmm].
b_{bf} = bottom flange width [mm].
I_s = moment of inertia [mm^4].
s = distance of bottom flange to centre of gravity sheet section [mm].

Because the internal and external bending moment should be equal, it can be derived that:

$$\frac{FL_{span}}{4} = \frac{F_{bf}I_s}{b_{bf}s*t} \Leftrightarrow F = \frac{4F_{bf}I_s}{L_{span}b_{bf}s*t} \tag{31}$$

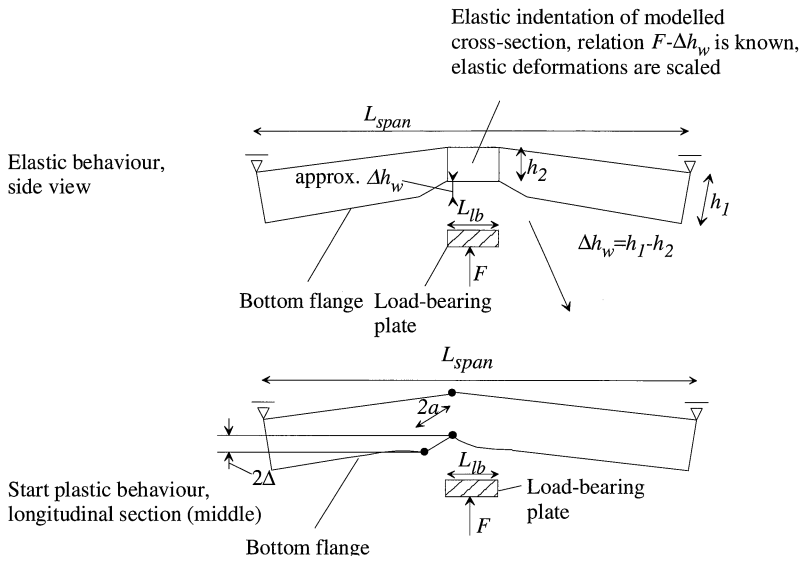

Fig. 16. Relationship between elastic cross-section deformation and plastic flip-disc deflection.

Intersection of elastic and plastic curves

Formula 28 can be substituted into formula 1 describing elastic sheet section behaviour. This results in the following:

$$F_e = \frac{EI(3b_{bf} + 2b_w)2\Delta}{r_{ibf}{}^2 \sin^2(\theta) b_w \left(b_{bf} - \frac{4}{3} r_{ibf} \sin(\theta_w)\right)} \tag{32}$$

Formula 27 can be substituted into formula 31.

This results in:

$$F_p = \frac{4F_{bf}I_s}{L_{span}b_{bf}s*t} * \tag{33}$$

$$\frac{f_y t b}{6}\left[1 - \frac{2\Delta}{t} + \sqrt{\left(\frac{2\Delta}{t}\right)^2 + 1} - \frac{6\Delta}{t\left(1+4a^2/b^2\right)} + 4\sqrt{\left(\frac{3\Delta}{2t\left(1+4a^2/b^2\right)}\right)^2 + 1}\right]$$

If the elastic load F_e and the plastic load F_p are set as equal, the flip-disc out-of-plane displacement can be solved. Then the ultimate sheet section load F_u can be calculated by using the value for Δ into formulae 32 or 33.

3.4 *Verification of post-failure models*

Experiments of section 2 are used failing by the yield arc post-failure mode. Table 1 shows the correlation, average, etc. for the experiments and Eurocode3 [9] predictions. Table 2 shows the experiments and the yield arc post-failure model predictions as presented in section 3.1.

Table 1. Eurocode3 predictions for experiments failing by the yield arc post-failure mode.

Experiments A (33)	Correlation (code,exp.)	Average (code/exp.)	Standard deviation (id.)	Coefficient of variation (id.)
Eurocode3	0.95	0.93	0.09	0.09

Table 2. Post-failure model predictions for experiments failing by the yield arc post-failure mode.

Experiments A (33)	Correlation	Average	Standard deviation	Coefficient of variation
Model MA1	0.70	1.32	0.36	0.27

Eurocode3 predictions are better than the post-failure model predictions. Section 4 will suggest some differences between Eurocode3 and the models as a possible cause for the differences in performance.

Experiments of Bakker's thesis [5] are used that are failing by the rolling post-failure mode. Furthermore, the 7 experiments of section 2 (failing by the rolling post-failure mode) are used. Table 3 shows the correlation, average, etc. for the experiments and Eurocode3 predictions. The ultimate load of the experiments F_{test} is used for the comparison, not the mode initiation load F_{imec}, because Eurocode3 predicts the ultimate load for sheet sections. In fact, almost all Bakker experiments do not satisfy the conditions for using Eurocode3 (see thesis [1] chapter 2 for more details). However, to have some possibilities to compare the Eurocode3 and the post-failure models, the experiments are still used.

Table 3. Eurocode3 predictions for experiments failing by the rolling post-failure mode.

Bakker experiments (28) and experiments section 2 (7)	Correlation	Average	Standard deviation	Coefficient of variation
Eurocode3	0.67	0.95	0.19	0.20

Table 4 shows the experiments and the rolling post-failure model as presented in section 3.2. Now, the mode initiation load F_{imec} is used for the comparison, because the post-failure models predict the mode initiation load.

Table 4. Post-failure model predictions for experiments failing by the rolling post-failure mode.

Bakker experiments (28) and experiments chapter 3 (7)	Correlation	Average	Standard deviation	Coefficient of variation
Model MR1	0.85	0.83	0.18	0.21

Model predictions are much better than the Eurocode3 predictions. However, Eurocode3 predicts the ultimate load, the post-failure models predict the mode initiation load.

Experiments of section 2 are used that failed by the yield eye post-failure mode. Table 5 shows the correlation, average, etc. for the experiments and Eurocode3 predictions. Table 6 shows the experiments and the yield eye post-failure model predictions as presented in section 3.3.

Table 5. Eurocode3 predictions for experiments failing by the yield eye post-failure mode.

Experiments E (7)	Correlation	Average	Standard deviation	Coefficient of variation
Eurocode3	0.87	0.91	0.10	0.11

Table 6. Post-failure model predictions for experiments failing by the yield eye post-failure mode.

Experiments E (7)	Correlation	Average	Standard deviation	Coefficient of variation
Model ME1	0.91	1.03	0.37	0.36

Both the Eurocode3 and the yield eye post-failure model predict the experimental values well. The standard deviation of the post-failure model is significantly higher than for Eurocode3. However, these conclusions are based on 7 experiments only.

The post-failure models presented cannot be used as design rules because their performance is less than the current design rule Eurocode3. Another mechanical model, using the same principles, has been developed to be a future design rule [3]. Section 4 will show that the post-failure models are usefull to increase the insight in sheeting behaviour.

4 Post-failure modes for changing variables

In section 3, a post-failure mechanical model was presented for each post-failure mode. Now, these three models are used for sheeting for which one variable value is changed. The mechanical model that predicts the lowest load is regarded as predicting the post-failure mode that is occurring. Every variable is presented in a separate section.

Section 3.4 shows that the averages of model predicted values divided by experimental values are not equal to 1.0. However, to compare predictions of the models, the averages had to be 1.0, which involves calibrating the models. The yield arc model predictions are divided by 1.32 (see table 2). The rolling model predictions are divided by 0.83 (see table 4) and the yield eye model predictions are divided by 1.03 (see table 6).

4.1 *Corner radius*

Experiments

Figures 4 and 8 in section 2 presented the post-failure mode for each experiment. Firstly, figures 4 and 8 indicate that for a larger corner radius (from 5 to 10 mm) a yield arc post-failure mode (A>R) changes into a rolling post-failure mode (R) (experiments 6 and 7-13). A yield arc post-failure mode followed by a rolling post-failure mode (A>R) was defined as a yield arc post- failure mode.

Secondly, the table indicates that a yield eye post-failure mode (E) changes into a yield arc post-failure mode (A) for larger corner radii. The changes of (A>E) into (A) point in the same direction: for small corner radii the yield arc post failure mode is still followed by a yield eye one (A>E), but for larger corner radii only a full yield arc post-failure mode occurs (A), experiments 55, 58, 59, and 68.

Post-failure mechanical models: yield arc into rolling

The three post-failure models are used for a sheet section with the following variable values. The corner radius r_{bf} changes between 1 and 15 mm. Other variables are fixed: b_{tf}=100 mm, b_w=100 mm, b_{bf}=100 mm, θ_w=90 degrees, L_{lb}=50 mm, L_{span}=600 mm, t=0.68 mm, f_y=340 N/mm^2.

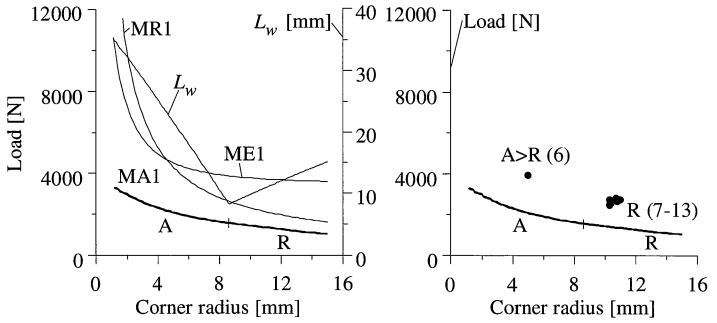

Fig. 17. Model predictions for changing corner radius, yield arc model (MA1), rolling model (MR1), and yield eye model (ME1).

Figure 17 shows the results. On the left, the model predictions are shown. It can be seen that the yield arc model (MA1) gives the lowest values for all corner radii. Thus, it is predicted that the yield arc post-failure mode occurs for all corner radii. However, for an increasing corner radius, model MA1 predicts smaller distances L_w (see figure 18). For corner radii larger than 8 mm, distance L_w even equals to the corner radius. This is also shown in figure 18. A yield arc post-failure mode then is quite similar to the rolling post-failure mode. This is also indicated by the curve of the rolling model (MR1), the model for the rolling post-failure mode. This curve converges to the curve of the yield arc model.

Figure 17 on the right shows the experimental ultimate loads of tests 6 and 7-13 (see also figure 4). For the rolling post-failure modes (R) the experimentally found mode initiation load is used, not the ultimate load. The same trend (for ultimate load / mode initiation values and post-failure modes) is followed as the post-failure models indicate.

Post-failure mechanical models: yield eye into yield arc.

The three post-failure models are used for a sheet section with the following variable values. The corner radius r_{bf} changed between 1 and 15 mm. Other variables are fixed: b_{tf}=100 mm, b_w=100 mm, b_{bf}=100 mm, θ_w=90 degrees, L_{lb}=100 mm, L_{span}=2400 mm, t=0.68 mm, f_y=340 N/mm^2.

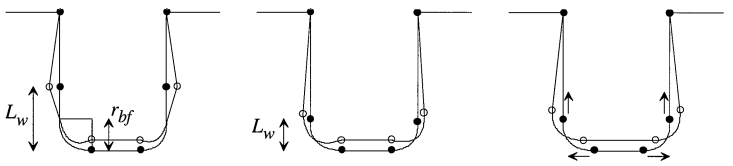

Fig. 18. A yield arc post-failure mode with a small distance L_w is quite similar to a rolling post-failure mode. Distance L_w cannot be smaller than the corner radius.

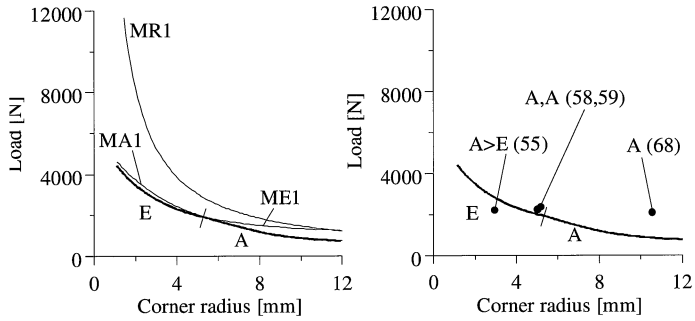

Fig. 19. Model predictions for changing corner radius II.

Figure 19 shows the results. On the left, the model predictions are shown. It can be seen that first the yield eye model gives the lowest values, followed by the yield arc model. Thus, it is predicted that first the yield eye post-failure mode occurs and then the yield arc post-failure mode. This is in accordance with the experimental findings.

Figure 19 on the right shows the experimental ultimate loads of tests 55, 58, 59, and 68 (see also figures 4 and 8). The same trend (for ultimate load values and post-failure modes) is followed as the post-failure models indicate.

Behavioural insight

Figures 17 and 19 show why a specific post-failure mode occurs for a certain value of the corner radius. However, to really understand why this is the case, it is important to know why the lines in the figure increase, decrease, or remain the same for different corner radii.

It was shown that for an increasing corner radius, a yield arc post-failure mode changes into a rolling post-failure mode. This because distance L_w (figure 18) decreases for an increasing corner radius. The mechanical model in [2], Appendix 4, section 4.3.1, explains why distance L_w decreases. The explanation is quite elaborate and will not be repeated here.

It was also shown that for an increasing corner radius, a yield eye post-failure mode changes into a yield arc post-failure mode. This is explained below.

All three models predict decreasing strength for an increasing corner radius. This can be explained because for a larger corner radius the elastic web crippling stiffness decreases. Because the ultimate load is predicted by intersection of the elastic and plastic curve, and the plastic curves are decreasing, the predicted ultimate load will decrease too.

It cannot be easily determined why the strength according to the yield arc model decreases slightly more strongly than the strength predicted by the yield eye model (the reason why for large corner radii the yield arc post-failure occurs).

Conclusions

Experiments show that for an increasing corner radius, a yield arc post-failure mode is followed by a rolling post-failure mode. Furthermore, they show that a yield eye post-failure mode is followed by a yield arc post-failure mode.

The post-failure mechanical models show that for an increasing corner radius, a yield arc post-failure mode is followed by a rolling post-failure mode. This because the yield arc model predicts a lower distance L_w. Why this model predicts a lower distance L_w is explained in [2], Appendix 4, section 4.3.1.

The post-failure mechanical models show that for an increasing corner radius, a yield eye post-failure mode is followed by a yield arc post-failure mode.

4.2 *Span length*

Experiments

Figures 4 and 8 show often that for a larger span length (A>R) changes into (A), experiments 1, 3, 22, and 24. This means that for a small span length a yield arc post-failure mode is followed by a rolling post-failure mode. For a larger span length a pure yield arc post-failure mode occurs.

For even larger span lengths (A) changes into (A>E), for instance experiments 43 and 55. This means that for larger span lengths, a pure yield arc post-failure mode changes into a yield arc post-failure mode followed by a yield eye post-failure mode. Sometimes, a pure yield eye post-failure mode occurs for long span lengths.

Post-failure mechanical models: rolling into yield arc

Unfortunately, it was not possible to find a set of sheet section variable values to show a change of the rolling into a yield arc post-failure mode for increasing span length.

Post-failure mechanical models: yield arc into yield eye

The three post-failure models are used for a sheet section with the following variable values. The span length L_{span} is changed between 600 and 2400 mm. Other variables are fixed: b_{tf}=100 mm, r_{bf}=3 mm, b_w=100 mm, b_{bf}=100 mm, θ_w=90 degrees, L_{lb}=100 mm, t=0.68 mm, f_y=340 N/mm^2. Figure 20 shows the results. On the left, the model predictions are shown. It can be seen that first the yield arc model (MA1) produces the lowest values, then the yield eye model (ME1). Thus, it is predicted that for increasing span length, the yield arc post-failure mode changes into a yield eye post-failure mode. This is in accordance with the findings of the experiments.

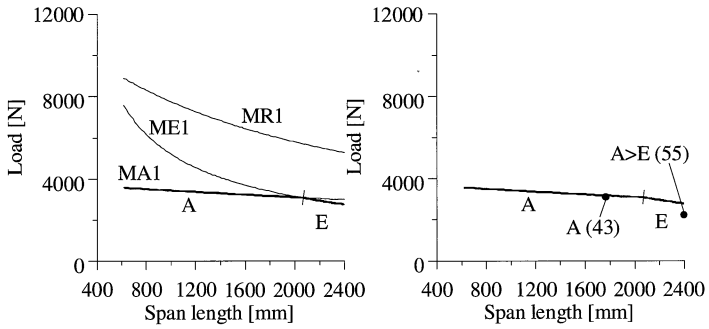

Fig. 20. Model predictions for changing span length.

Figure 20 on the right shows the experimental ultimate loads of tests 43 and 55 (see also figures 4 and 8). The same trend for ultimate load values and post-failure modes is observed as the post-failure models indicate.

Behavioural insight

For long span lengths, the stresses in the bottom flange increase strongly. Therefore the plastic load for the yield eye model is reached more easily. Although the rolling and yield arc post-failure mechanical models decrease in strength (due to the length factor), this effect is not as strong as the influence of increasing stress for the yield eye model.

Conclusions

Experiments show that for an increasing span length, a yield arc post-failure mode is followed by a yield eye post-failure mode. Furthermore, they suggest that a rolling post-failure mode is followed by a yield arc post failure mode. The post-failure mechanical models show results in accordance with the experiments.

4.3 *Angle between web and flange*

Experiments

Figures 4 and 8 show that for an increasing angle between web and flange (A>R) changes into (R), experiments 7-13 and 14. Furthermore, (A) changes into (A>E) and (E), experiments 40, 41, 56, and 57. This means that, for an increasing angle, the yield arc post-failure mode changes into a yield eye or a rolling post-failure mode.

Post-failure mechanical models: yield arc into yield eye

Unfortunately, it was not possible to find a set of sheet section variable values to show a change of a yield arc into a yield eye post-failure mode for increasing angle between web and flange.

Post-failure mechanical models: yield arc into rolling

Post-failure models MA1, MR1, and ME1 are used for a sheet section with the following variable values. The angle between web and flange θ_w changes between 50 and 90 degrees. Other variables

are fixed: b_{tf}=100 mm, r_{bf}=10 mm, b_w=100 mm, b_{bf}=100 mm, L_{lb}=50 mm, L_{span}=50 mm, t=0.68 mm, f_y=340 N/mm^2. Figure 21 shows the results. On the left, the model predictions are shown. It can be seen that the yield arc model (MA1) always gives the lowest values. However, distance L_w in the yield arc model decreases until the corner radius value is reached. Similar to the situation for the changing corner radius, it is then likely that the yield arc model predicts a rolling post-failure mode. Thus, the sequence is a yield arc followed by a rolling post-failure mode. This is in accordance with the findings of the experiments. Figure 21 on the right shows the experimental ultimate loads of tests 7-13 and 14 (see also figures 4 and 8). The same trend for ultimate load values and post-failure modes is followed as the post-failure models indicate.

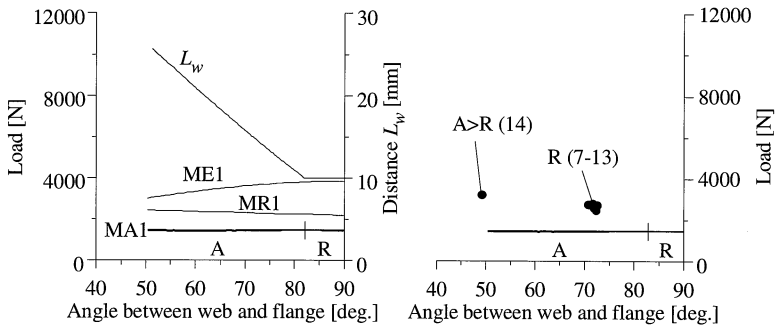

Fig. 21. Model predictions for changing angle between web and flange.

Behavioural insight

For an increasing angle between web and flange, the stiffness of the cross-section decreases (see formula 1) which results in lower ultimate loads. This is true for both the yield arc and rolling models.

However, for the yield arc model, formulae in [2], Appendix 4, section 4.3.1 can be used to show that distance L_w reduces, resulting in higher ultimate loads. As figure 21 shows, the decrease of cross-section stiffness and reduction of distance L_w more or less compensate each other with a constant ultimate load.

For the rolling model there is another explanation for decreasing ultimate loads for increasing angle. Figure 22 shows that if the angle between web and flange $\theta_w < 90$ degrees, deformation of the cross-section leads to the web pushing the bottom flange downwards. This downward movement is in the opposite direction to the direction in which the force is working. Thus, smaller angles increase the load.

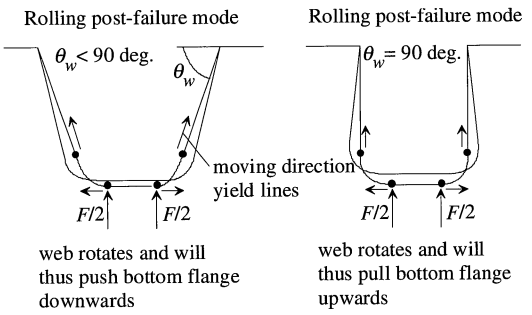

Fig. 22. *For the rolling post-failure mode, an angle between web and flange causes the web pushing the bottom flange downwards, thus increasing the load.*

Conclusions

Experiments show that for an increasing angle between web and flange, a yield arc post-failure mode is followed by a rolling post-failure mode. Furthermore, they show that a yield arc post-failure mode is followed by a yield eye post-failure mode.

The post-failure mechanical models also show that a yield arc post-failure mode is followed by a rolling post-failure mode. This because the distance L_w will reduce for larger angles between web and flange. An explanation why this distance shows reduction is too elaborate to explain here, but formulae in [2], Appendix 4, section 4.3.1 can be used to show this.

4.4 *Load-bearing plate width*

Experiments

Figures 4 and 8 show that for an increasing load-bearing plate width a yield arc post-failure mode (A) changes into a yield arc followed by a yield eye post-failure mode (A>E), experiment 71 and 72. This indicates that for increasing load-bearing plate width, a yield arc post-failure mode is followed by a yield eye post-failure mode.

Post-failure mechanical models: yield arc into yield eye

The three post-failure models are used for a sheet section with the following variable values. The load-bearing plate width L_{lb} is changed between 50 and 150 mm. Other variables are fixed: b_{tf}=100 mm, r_{bf}=10 mm, b_w=100 mm, b_{bf}=100 mm, θ_w=50 degrees, L_{span}=2400 mm, t=0.68 mm, f_y=340 N/mm^2.

Figure 23 shows the results. On the left, the model predictions are shown. It can be seen that first the yield arc model (MA1), then the yield eye model (ME1) gives the lowest values. Thus, the sequence is a yield arc followed by a yield eye post-failure mode. This is in accordance with the findings of the experiments.

Figure 23 on the right shows the experimental ultimate loads of tests 71 and 72 (see also figures 4 and 8). The same trend for ultimate load values and post-failure modes is observed as the post-failure models indicate.

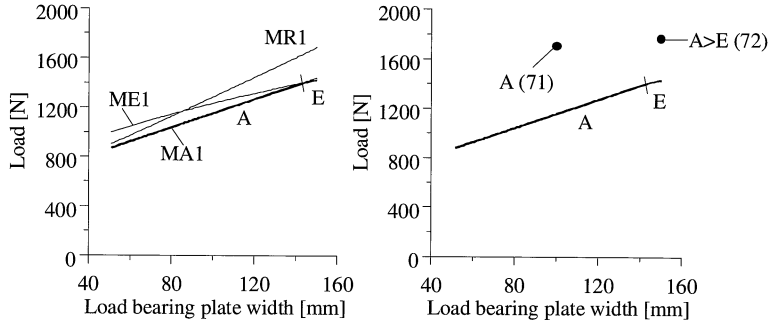

Fig. 23. Model predictions for changing load-bearing plate width.

Behavioural insight

Figure 23 on the left shows that for a decreasing load-bearing plate width, the rolling model values decrease more than the yield arc model values. If the lines were to cross, this would suggest a rolling to a yield arc post-failure mode sequence. Unfortunately, there are no experiments that can prove this suggestion.

If the load-bearing plate width increases, the rolling and yield arc models increase their values, because the modelled cross section (see figure 9) is wider. But the yield eye model (ME1) is not sensitive to increasing the load-bearing plate width, see formulae 32 and 33. Finally, the yield eye model predicts lower values than the yield arc model.

Conclusions

Experiments suggest that for an increasing load-bearing plate width, a yield arc post-failure mode is followed by a yield eye post-failure mode. The post-failure mechanical models also show that a yield arc post-failure mode is followed by a yield eye post-failure mode. This is because for the yield eye post-failure mode, only the bending moment in the section reduces due to the larger load-bearing plate width. For the yield arc post-failure mode, the modelled cross-section is larger.

5 Conclusions

New experiments have been carried out in which sheet sections were loaded by concentrated load and bending moment. The experiments showed that after ultimate load, three post-failure modes occur.

Mechanical models have been developed for all three post-failure modes. The models do not perform as good as Eurocode3, but they can be used to increase insight in sheeting behaviour.

For some sheet section variables, namely the corner radius, span length, angle between web and flange, and the load-bearing plate width, experiments and the post-failure mechanical models predict the same sequence of post-failure modes for a changing variable. The mechanical models provide insight into why a specific post-failure mode occurs.

Acknowledgements

This research was supported by the Technology Foundation STW, applied science division of NWO and the technology programme of the Ministry of Economic Affairs in The Netherlands.

Literature

[1] HOFMEYER, H.: Combined Web Crippling and Bending Moment Failure of First-Generation Trapezoidal Steel Sheeting, Ph.D.-thesis, Eindhoven University of Technology, Faculty of Architecture, Department of Structural Design, ISBN 90-6814-114-7, The Netherlands, 2000.
[2] HOFMEYER, H.: Report TUE-BCO-00-09: Report on Combined Web Crippling and Bending Moment Failure of First-Generation Trapezoidal Steel Sheeting (Appendices to the thesis), Eindhoven University of Technology, Faculty of Architecture, Department of Structural Design, The Netherlands, 2000, ISBN 90-6814-115-5.
[3] HOFMEYER, H.; KERSTENS, J.G.M.; SNIJDER, H.H.; BAKKER, M.C.M.: New Prediction Model for Failure of Steel Sheeting Subject to Concentrated Load (Web Crippling) and Bending, submitted to Thin-Walled Structures.
[4] HOFMEYER, H.; KERSTENS, J.G.M.; SNIJDER, H.H.; BAKKER, M.C.M.: Combined Web Crippling and Bending Moment Failure of First-Generation Trapezoidal Steel Sheeting, submitted to Journal of Constructional Steel Research.
[5] Bakker, Monique C.M.: Web Crippling of Cold-Formed Steel Members, Dissertation Eindhoven University of Technology, The Netherlands, ISBN 90-386-0122-0, 1992.
[6] Vaessen, M.J.: On the elastic web crippling stiffness of thin-walled cold-formed steel members, MSc. thesis, Eindhoven University of Technology, Department of Structural Design, The Netherlands, 1995.
[7] BAKKER, M.C.M., SNIJDER, H.H., KERSTENS, J.G.M. Elastic Web Crippling of Thin-Walled Cold Formed Steel Members. Proceedings Light-Weight Steel and Aluminium Structures, Fourth International Conference on Steel and Aluminium Structures, Mäkeläinen, P; Hassinen, P., June 1999, Espoo, Finland.
[8] MURRAY, N.W.; KHOO, P.S.: Some Basic Plastic Mechanisms in the Local Buckling of Thin-Walled Steel Structures, International Journal of Mechanical Science, Vol. 23, No. 12, page 703-713, 1981.
[9] ENV 1993-1-3, European Prestandard Eurocode3, Design of Steel Structures, Part 1-3: General rules-Supplementary rules for cold-formed thin gauge members and sheeting, European Committee for Standardisation CEN, Brussels, April 1996.